Modification of energetic modes for transitional flow control

Arnob Das Gupta and Subrata Roy

COLLECTIONS

F This paper was selected as Featured

View Online   Export Citation   CrossMark

AIP Advances
SPECIAL TOPIC: Advances in Low Dimensional and 2D Materials

Call For Papers!

Modification of energetic modes for transitional flow control Ⓕ

View Online   Export Citation   CrossMark

Arnob Das Gupta ⓘ and Subrata Roy[a] ⓘ

AFFILIATIONS

Applied Physics Research Group, Department of Mechanical and Aerospace Engineering, University of Florida, Gainesville, Florida 32611, USA

[a]Author to whom correspondence should be addressed: roy@ufl.edu

ABSTRACT

We introduce a mechanism of using collocated serpentine shaped plasma actuators for controlling the flow via an input electrical signal to either advance or delay transition by amplification or annihilation of energetic modes of turbulent structures. A wall resolved implicit large eddy simulation is conducted to examine the process of turbulent flow control due to this mechanism. Collocation allows for selective superposition of different energetic modes, which can either subtract or add energy to the baseline flow resulting in turbulent streak manipulation. Unlike most flow control methods that use either a localized large amplitude forcing or a low amplitude distributed forcing, this mechanism uses a localized low amplitude forcing to cause reduction in skin friction of more than 53% across the plate. This is achieved by manipulating strength as well as the spacing between the low-speed turbulent streaks, which are ubiquitous in a turbulent flow field. Reduction in skin friction drag can result in decreasing fuel consumption and in turn reducing pollution.

INTRODUCTION

Flow control can be achieved by either reducing or increasing the turbulence production. The turbulent production is associated with Reynolds stress in a turbulent flow field. In a wall-bounded turbulent flow, Reynolds stress brings fast-moving fluid toward the wall (sweeping event) and slow-moving fluid away from the wall (ejection event). These events are generally associated with streamwise vortices, which are closely related to elongated low-speed streaks near the wall (Schoppa and Hussain, 2002). These streaks, also called Klebanoff modes (Kendall, 1985), are fluctuations arising from low-frequency filtering of freestream perturbations (Klebanoff, 1971 and Goldstein, 2014) by the boundary layer. In a transitional flow, these streaks exhibit algebraic or transient growth (Matsubara and Alfredsson, 2001) and lead to bypass transition due to their non-modal nature (Andersson et al., 1999). This type of mechanism is commonly found in pipe flow (Wu et al., 2015) and turbomachinery applications (Wheeler et al., 2016). The two significant mechanisms by which streaks break down are via sinuous and varicose modes (Schoppa and Hussain, 2002), which can be either fundamental or subharmonic in nature. Manipulating the strength and spacing between these streaks can significantly reduce drag on a surface. Drag reduction greater than 30% (Du and Karniadakis, 2000) was obtained by manipulating the streaklines using spanwise oscillating Lorentz force in a channel flow (Du and Karniadakis, 2000 and Altıntaş and Davidson, 2017). Using similar principles, plasma actuators were found to reduce drag by 45% (Choi et al., 2011). However, these large reductions were associated with either a distributed actuation of low perturbation amplitude (Du and Karniadakis, 2000) or a localized high perturbation amplitude (Choi et al., 2011) relative to the bulk flow. A single localized flow control device that can adapt to the situation where the streaks need to be favorably manipulated to accentuate or mitigate turbulence in aerodynamic applications has not been studied before.

Surface Dielectric Barrier Discharge (SDBD) plasma actuators have increased in prevalence as active flow control devices over the last three decades (Wang et al., 2013). These actuators are surface compliant, have a rapid response time with no moving parts, and can be applied at receptive locations. The standard design involves two asymmetrically placed electrodes, one exposed and the other encapsulated, separated by a dielectric material (Roth et al., 2000). A high voltage (~kV) alternating current (~kHz) is applied to the electrodes

across the dielectric material, which ionizes the air surrounding the exposed electrode. Due to asymmetry of the electrodes, the electric field accelerates the ionized particles in the required direction, generating a wall jet via a Lorentzian collisional mechanism, which can be used to manipulate the background flow field.
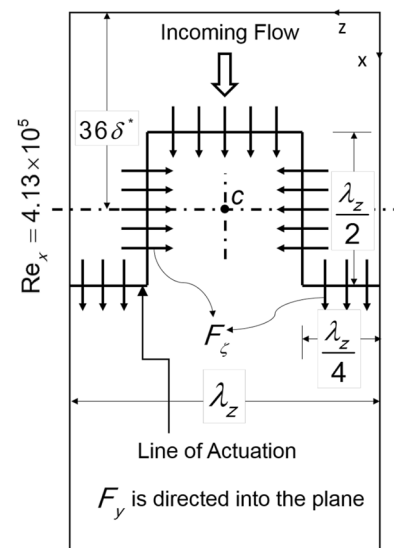
This report investigates numerically the use of square serpentine shaped plasma actuators (Durscher and Roy, 2012) to control turbulent transition by modifying strength and spacing between the streaks. For the numerical investigation, a wall resolved implicit large eddy simulation is conducted to study the impact of collocation of square serpentine plasma actuators on a background laminar flow over a zero-pressure gradient flat plate. This study shows how the Klebanoff modes or streaks can be accentuated or mitigated by using a localized forcing of small amplitude. Plasma actuators have been used to control transitional flow by manipulating Tollmien–Schlichting (T–S) waves (Grundmann and Tropea, 2008). However, in most practical aerodynamic applications, free stream turbulence levels are not low enough for T–S wave transition. Therefore, the present work concentrates on non-modal bypass transition. We show here that unlike most flow control devices, serpentine shaped actuators can be used to advance or delay the transition to turbulence by simply changing the input signal and hence can control drag, reduce noise, improve turbulent mixing, or control flow separation.

NUMERICAL METHOD

The governing equations are unfiltered compressible Navier–Stokes equations (Houba *et al.*, 2019). The modal discontinuous Galerkin method is used as an implicit large eddy simulation (ILES) tool to simulate the turbulent flow field. This code is implemented in our in-house code called Multiscale Ionized Gas (MIG) flow code (Bhatia *et al.*, 2014 and Houba *et al.*, 2019). We use a third-order accurate spatial scheme with fully explicit two-step Runge–Kutta time discretization. For temporal resolution, a non-dimensional time step of $\Delta t^+ = u_{\tau,i}^2 \Delta t / \nu = 0.0048$ was used, where $u_{\tau,i}^2$ is the inlet friction velocity and ν is the kinematic viscosity. The flow was allowed to convect two times over the entire streamwise length at a convective speed of around $0.75 U_\infty$, before the mean flow calculations were started. The mean flow calculations were done as the flow convected once over the entire streamwise length. Local Lax–Friedrichs flux was used for the convective numerical flux, and the local discontinuous Galerkin method is used for viscous fluxes (Bassi *et al.*, 2005).

The Mach number of the incoming flow is set to 0.5. The freestream conditions are applied with a static pressure (P_∞) of 10 132.5 Pa and a static temperature (T_∞) of 273 K. The freestream velocity (U_∞) is 165.61 m/s, and the dynamic viscosity (μ_∞) based on Sutherland's law is 1.716×10^{-5} Ns/m^2. A Blasius profile corresponding to the Reynolds number, $Re_x = 3.75 \times 10^5$, is used for the streamwise and wall normal velocity at the inlet. The wall is kept at no slip adiabatic conditions. Both top and outlet boundary conditions are obtained by linear extrapolation with the pressure kept at P_∞. The domain is periodic in the spanwise direction.

The streamwise (x direction), wall normal (y direction), and spanwise (z direction) domain sizes correspond to $400\delta^*$, $59\delta^*$, and $15\delta^*$, respectively, where δ^* is the inlet displacement thickness. A mesh size of $750 \times 64 \times 64$ is used to resolve the flow. The
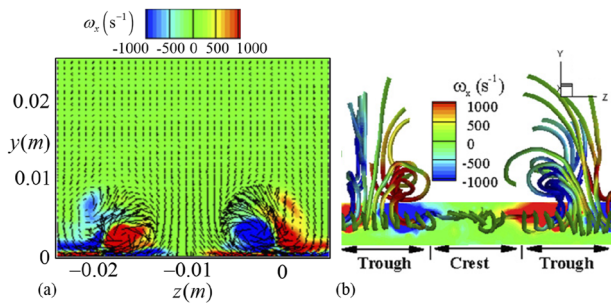

FIG. 1. Schematic of the square actuator design. The forcing terms are applied in the arrow directions. The wavelength of the actuator λ_z also defines the spanwise extent of the domain. A similar procedure is used for the control actuator.

mesh is uniform in the streamwise and spanwise directions, and it is stretched in the wall normal direction. The top and outlet boundary elements are stretched to avoid reflections. For mesh convergence, different mesh sizes were chosen with the mesh size in the wall normal direction ranging from 48 to 64 and in the spanwise direction ranging from 32 to 64. The convergence study showed that the mesh size of $750 \times 48 \times 64$ was adequate to resolve the rms fluctuations when compared to DNS results.

The actuator is placed at $36\delta^*$ from the inlet. The forcing function is modified from Singh and Roy (2008) for general coordinates as given in Eq. (S1) and Eq. (S2) in the supplementary material. The forcing terms are applied along the line of actuation shown in Fig. 1. The control actuator locations are shown in Table S1 in the supplementary material. The parameter A of Eq. (S2) is obtained by applying the forcing in quiescent conditions, and the value of A for which the maximum mean velocity magnitude generated is 10% of the freestream is chosen. More details on the actuation as well as the transition mechanism have been described earlier (Das Gupta and Roy, 2017).
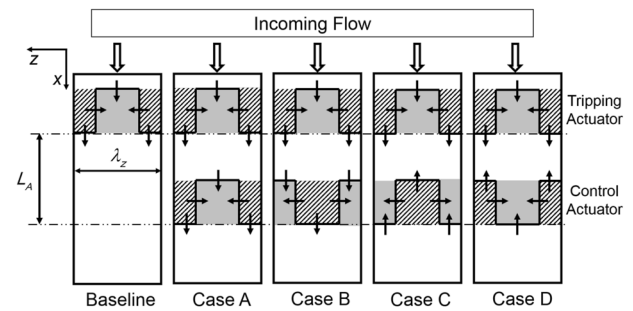
PROBLEM SPECIFICATION

In a transitional flow, the streak locations are random, which makes it difficult to apply most flow effectors that may suppress or accentuate turbulence production depending on the application. Serpentine actuators are known to produce three-dimensional flow structures (see Fig. 2) that can enhance plasma coupling with the flow. A flow visualization picture shows bundling of random streaklines into a "predictable" arrangement (Fig. 3, experimental details in the supplementary material), allowing a control actuator to selectively manipulate them. This is an exciting approach where a turbulence control methodology with known near wall forcing

FIG. 2. (a) Time averaged contours of streamwise oriented bound vortical structures on a y–z plane 12.5 mm from the beginning of the actuator and (b) corkscrew-like structures of streamtraces colored with vorticity induced by square serpentine actuators (Durscher and Roy, 2012). Reproduced with permission from R. J. Durscher and S. Roy, "Three dimensional flow measurements induced from serpentine plasma actuators in quiescent air," J. Phys. D: App. Phys. **45**, 035202 (2012). Copyright 2012 IOP Publishing Ltd.

FIG. 4. Schematic of various control actuator configurations relative to the tripping actuator. The domain is periodic in the z direction (spanwise). The shaded gray regions are the pinching region of the actuators where the force vectors, shown as arrows, point toward each other. The hatched regions correspond to the spreading region where force vectors point away from each other. The control actuator is located at a distance L_A from the tripping actuator (Table S1). Based on the direction of forces, which are parallel to the streamwise direction, the control actuators for cases A and B are in co-flow arrangement and cases C and D are in counter-flow arrangement.

can be introduced without flow sensing so that the dominant structures can be bundled in a deterministic fashion, so are the turbulent events. Therefore, we propose to perturb the flow using the tripping actuators shown in Fig. 4 to manipulate the incoming random streaklines, which may then be manipulated by another set of actuators to control transition as needed. The actuator body force is numerically implemented from force approximation based on first principles modeling (Singh and Roy, 2008). The forcing method, numerical details, and mesh parameters (supplementary material) are the same as those used in Das Gupta and Roy (2017). The cases studied vary in the arrangement of the control actuator, with both the pinch regions aligned or pinch and spread regions aligned for the tripping and control actuator. The tripping and the control actuator are forced at the same sinusoidal frequency of 1 kHz and amplitude based on velocity ratio $\gamma = u_p/U_\infty = 0.1$, where u_p is the maximum mean velocity magnitude generated by the actuator in quiescent conditions and U_∞ is the freestream velocity. This gives a root mean square velocity of the forcing to be around 7% of the freestream velocity. The distance between the actuators scaled by viscous units $L_A = u_\tau \Delta x / \nu$, where Δx is the distance between two actuators, u_τ is the maximum friction velocity for the baseline case, and ν is the
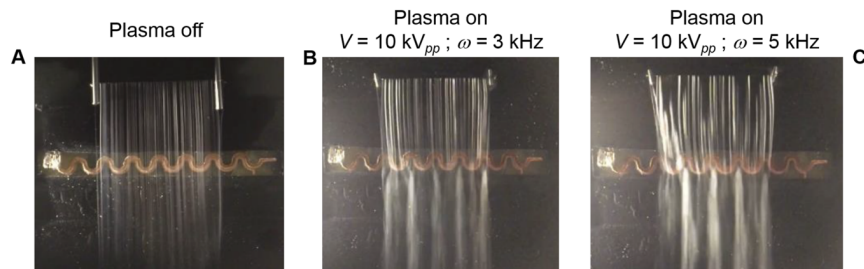
freestream kinematic viscosity. The control actuators for cases B and D are shifted by $\lambda_z/2$ (Fig. 1) in comparison to cases A and C, respectively.
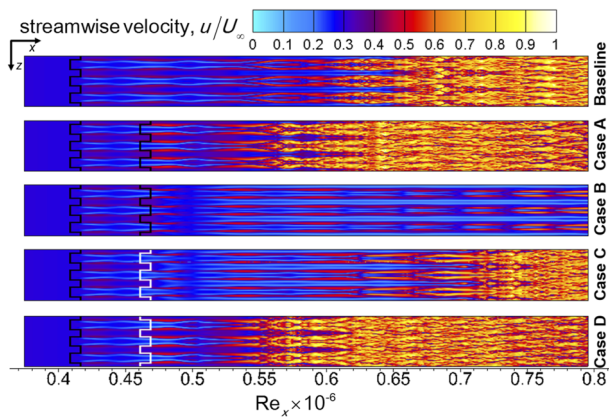
RESULTS AND DISCUSSION

The streaklines displayed in Fig. 5 at $y/\delta^* \approx 0.5$, where δ^* is the displacement thickness, show the subharmonic sinuous nature (Schoppa and Hussain, 2002 and Das Gupta and Roy, 2017) for all the cases. Cases B and C distribute the energy in the spanwise direction and create additional low-speed streaks by doubling their spanwise wavenumber. This reduces the spanwise streak spacing and therefore the amplitude of the sinuous wavy streak, which makes them more parallel in comparison to the baseline case. Although case C is in a counter-flow arrangement, which creates an inflection region in the boundary layer and should destabilize the flow (Riherd et al., 2014), it delays the transition. This denotes that the pinch and spread behavior of the control actuator can overcome the inviscid instability arising from counter-flow and still delay the transition.

FIG. 3. Smoke flow visualization study of a transitional flow affected by a circular serpentine plasma actuator (Wilkinson 2017). The wind tunnel is operated at 450 rpm (~6 m/s). The wavelength of the electrodes is 10.16 mm, and the width of the electrode is 1 mm. The unit Reynolds number ranges from $0.5 \times 10^6 < Re/m < 3.3 \times 10^6$. The smoke was generated using a high voltage AC current applied across the wire applied with a mixture of oil (~85% by volume) and soap (~15%). (a) Plasma actuator is turned off, (b) plasma actuator is run at a voltage $V = 10 \text{ kV}_{pp}$ and frequency $\omega = 3$ kHz, and (c) plasma actuator is run at a voltage $V = 10 \text{ kV}_{pp}$ and frequency $\omega = 5$ kHz.
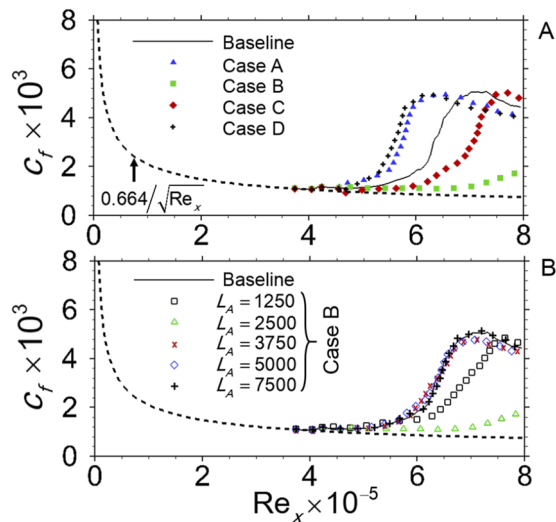
FIG. 5. Comparison of normalized instantaneous streamwise velocity contours depicting streaklines in the $y/\delta^* \approx 0.5$ plane. The domain is duplicated three times in the spanwise direction. Actuators colored in black have co-flow arrangement, and those in white have counter-flow arrangement. The increase in the streak strength for cases A and D advances the transition, while the decrease in the streak strength as well as spacing delays transition for cases B and C.

Cases A and D add energy to the existing streaklines downstream of the control actuator and advance the transition.

The delay or advance in transition by different cases is depicted in the skin friction plots shown in Fig. 6. Cases A and D advance the transition location, while cases B and D delay the transition. The flow does not become fully turbulent in the chosen domain for case B. Case B, with the control actuator at $L_A = 2500$, reduces the skin friction along the plate by more than 53% (Table S2 in the supplementary material). The transition location is determined using the shape factor $H = \delta^*/\theta$ variation along the streamwise direction (Fig. 7), where θ is the momentum thickness. The transition location x_{tr} is defined as the location where the shape factor crosses the value of 1.4, which is typical of turbulent boundary layers (Schlichting, 1979). The Reynolds number at the transition location is given by $Re_{tr} = x_{tr}U_\infty/\nu$. Cases A and D both have $Re_{tr} \approx 6.4 \times 10^5$, and for case C, $Re_{tr} \approx 7.75 \times 10^5$ in comparison to the baseline with $Re_{tr} \approx 7 \times 10^5$. Therefore, transition delays of 10% (case C) and advance of 8.5% (case A) can be achieved by altering the direction of the plasma body force or input signal.

From an experimental point of view, this can be easily achieved by switching the electric field direction between the exposed and encapsulated electrodes. The parameter L_A is varied from 1250 to 7500 for case B to investigate how the location of the control actuator impacts the baseline flow [Fig. 6(b)]. The location closest to the tripping actuator with $L_A = 1250$ delays transition by 8.5%, while the locations beyond $L_A = 3750$ have insignificant difference in the transition location. Therefore, there is an optimal location where the control actuator should be placed to have the maximum impact on the flow. This location depends on the forcing frequency, which determines the duration for which the flow structures generated exist, and the freestream velocity, which determines how the flow structures get stretched due to their inclination (Das Gupta and Roy, 2017).

In Fig. 8, comparison of the excited Fourier components of the normalized streamwise fluctuations u'/U_∞ between baseline, case A, and case B is depicted. The plots are constructed using 21 x-planes in the transitional region. Discrete Fourier transform of
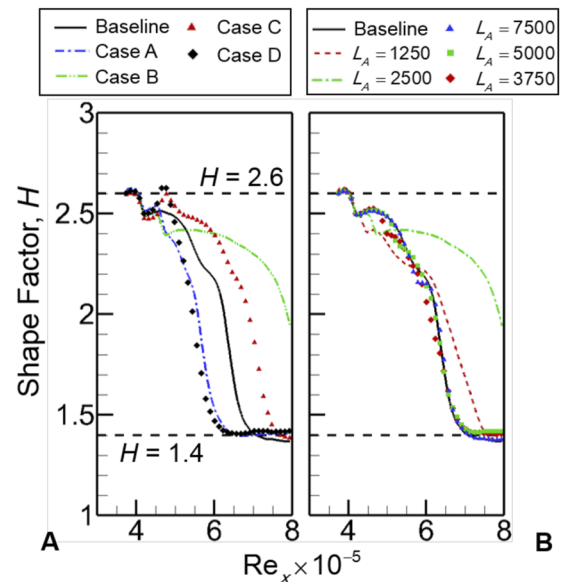

FIG. 6. Variation of the skin friction with the Reynolds number based on the control actuator configuration and location. (a) Comparison of skin friction with baseline for different cases with the control actuator at $L_A = 2500$. (b) Effect on transition with a change in the location of the control actuator for case B. Skin friction profiles left to the baseline case indicate transition advance, while those to the right indicate transition delay. The transition is complete after the skin friction reaches a peak and starts decreasing.
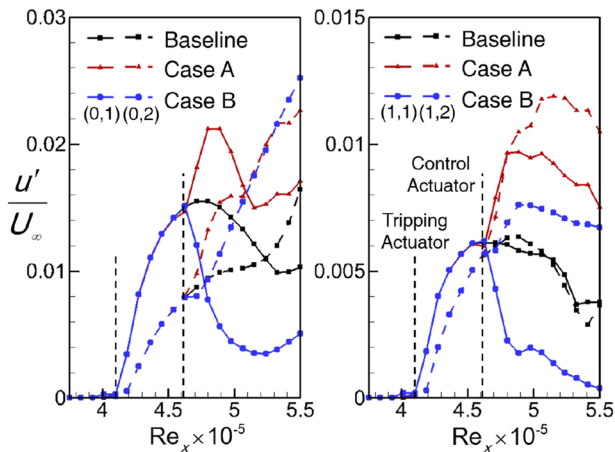

FIG. 7. Variation of the shape factor with the Reynolds number based on the control actuator configuration and location. (a) Comparison of the shape factor with baseline for different cases with the control actuator at $L_A = 2500$. (b) Effect on transition with a change in the location of the control actuator for case B. Every 20th grid point is shown.
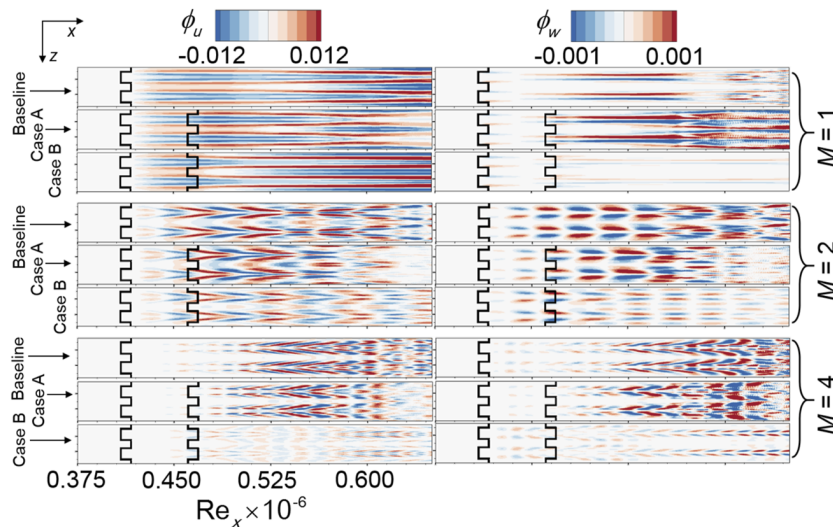
FIG. 8. Comparison of normalized streamwise fluctuation amplitudes for different (ω, β)-modes. Case A increases the amplitude for all the (ω, β)-modes after the control actuator location. Case B reduces the amplitude for (0, 1) and (1, 1)-modes, but increases it for (0, 2) and (1, 2)-modes.
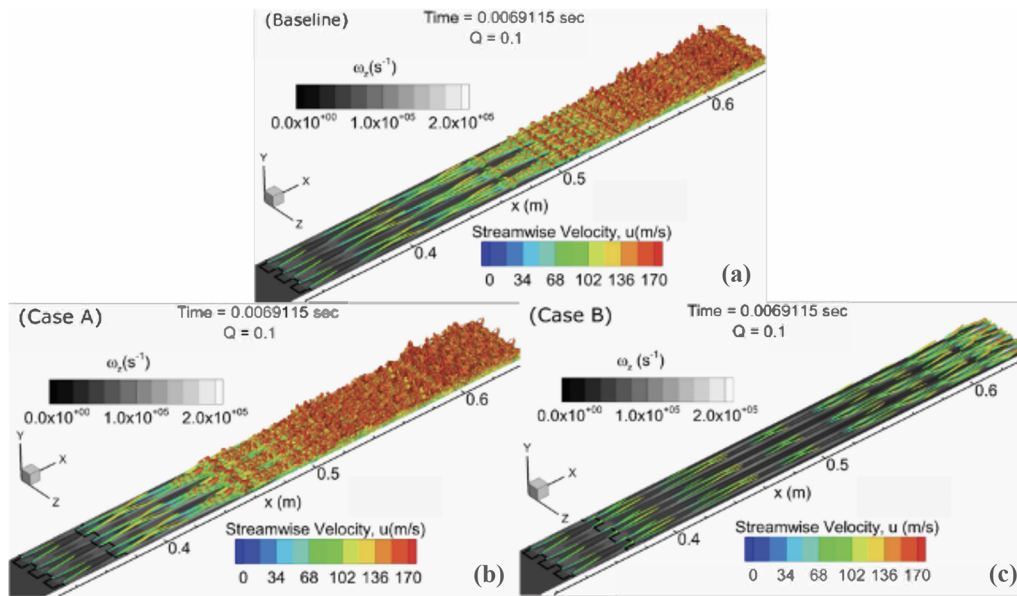
the fluctuations in an x-plane provides the maximum energy component for a specific spanwise mode β. The variation in time of this particular β mode provides the frequency ω. The combination ω, β shown in parentheses is normalized with the actuator frequency and wavenumber, respectively. The oblique mode corresponds to the (1, 1)-mode. The (0, 1)-mode has a higher amplitude than the (0, 2)-mode for $\text{Re}_x < 5.25 \times 10^5$, after which the nonlinear effects add energy to the higher wavenumber mode and cause the amplitude

of the (0, 2)-mode to be higher than the (0, 1)-mode. This location is advanced for cases A and B to $\text{Re}_x \approx 4.75 \times 10^5$. Since case A increases the fluctuation amplitude for all the (ω, β)-modes, the transition location is advanced. However, case B reduces the amplitude for the most energetic mode (0, 1) as well as the oblique mode (1, 1), which results in transition delay. Case B increases the amplitude for (0, 2) and (1, 2)-modes, supporting the doubling of the spanwise streak wavenumber observed in Fig. 5(c). For case B, the (ω, β)-modes for $\beta > 2$ have amplitudes that are lower than or similar to those of the baseline. Therefore, distributing energy between different modes results in transition delay for case B.

Since the flow is composed of superimposed coherent structures with different energy contents, a proper orthogonal decomposition (POD) of the flow field is used to analyze the energy content of these structures. It should be noted that POD modes comprise multiple (ω, β)-modes. The procedure followed is the snapshot method (see the supplementary material) proposed by Sirovich (1987). The streamwise (ϕ_u) and spanwise (ϕ_w) POD mode contours for a wall normal plane in the buffer layer are shown in Fig. 9. The highest energy containing mode ($M = 1$) has the same spanwise wavenumber as the actuation but the streamwise wavenumber is zero indicating a steady mode. The strength of ϕ_w ($M \geq 1$) and ϕ_u ($M > 1$) increases after the control actuator for case A and decreases for case B. For case A, the sum of the relative energy for all the modes greater than 5 (Tables S3 and S4) is around 10% more than the baseline. This suggests that the collocation of actuators in case A amplifies the energy of the higher modes by reducing it for the lower modes. For $M = 1$ in case B, the strength of ϕ_u is increased since majority of the energy from higher modes ($M > 1$) are transferred into $M = 1$, reducing the nonlinear interaction between the modes. The staggered pattern of positive and negative ϕ_w observed

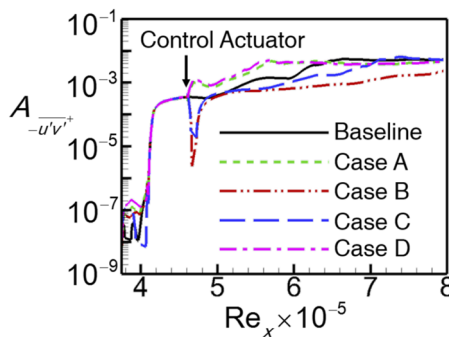

FIG. 9. Relative energy content for different energetic modes based on POD analysis. The contours are plotted for $y/\delta^* \approx 1$. The domain is duplicated two times in the spanwise direction. The contours are normalized to maintain a similar magnitude after the tripping actuator for all the cases. The increase or reduction in the energy of the POD modes relative to the baseline case results in advance or delay in transition, respectively. In case A, the lambda structures are stronger and the spacing between the legs of the structures decreases near the tip, while case B does the opposite. This phenomenon manipulates the spanwise oriented vortices near the tip of the lambda structures, where the streaks have maximum lift and are unstable, and they contribute to the advancement or delay in transition.

FIG. 10. Instantaneous plots of the Q-criterion at t = 0.006 911 5 s colored by the streamwise velocity show the effect of amplification and attenuation of energetic modes on enhancing and delaying flow transition to turbulence, respectively. (a) Baseline (Multimedia view), (b) Case A (Multimedia view), and (c) Case B (Multimedia view). Multimedia views: (a) https://doi.org/10.1063/5.0078083.1; (b) https://doi.org/10.1063/5.0078083.2; (c) https://doi.org/10.1063/5.0078083.3

in $M = 2$ corresponds to the oblique mode (Das Gupta and Roy, 2017 and Berlin *et al.*, 1994). For case A, the lambda vortices ($M = 2$, ϕ_u) grow. However, case B creates weak lambda structures ($M = 2$, ϕ_u) between the strong ones after $Re_x \approx 5.25 \times 10^5$, thereby doubling the spanwise wavenumber. These weak structures gradually become stronger relative to the upstream lambda vortices as the Reynolds number increases. This exchange of energy between the structures and the increase in the spanwise wavenumber lead to transition delay for case B.

The growth parameter $\overline{\psi(x,y)}$ is defined in Eq. S(7) of the supplementary material. Figure 10 shows instantaneous perspective plots of the Q-criterion colored by the streamwise velocity at t = 0.006 911 5 s, demonstrating the effect of amplification and attenuation of energetic modes on enhancing and delaying flow transition to turbulence, respectively. Transient evolutions of these plots are shown as supplementary movies in Figs. 10(a)–10(c) (multimedia view) for baseline, case A, and case B, respectively. The growth parameter (7) for Reynolds shear stress depicted in Fig. 11 shows that the control actuator for case B reduces the local Reynolds stress by two orders of magnitude compared to the baseline case. Both cases B and C reduce the growth in the Reynolds shear stress, while cases A and D increase the Reynolds stress. The change in the Reynolds stress will alter the turbulent transport and production.

CONCLUSION

In summary, collocation of plasma actuators can be used to selectively manipulate the streaklines to advance or delay transition by altering streak strength and spacing. Aligning pinch planes of the tripping and control actuator adds energy to the existing streaklines and advances the transition. However, aligning pinch and spread planes reduces the energy in the existing streaklines and distributes it along the spanwise direction by doubling the spanwise wavenumber, resulting in transition delay. Using localized finite amplitude forcing, a skin friction reduction of more than 53% can be achieved by reducing the strength of streamwise vortical structures, causing a reduction in the Reynolds shear stress and therefore turbulent

FIG. 11. Comparison of Reynolds shear stress growth parameters for different configurations. The collocation of actuators with the pinch plane aligned adds Reynolds shear stress at the control actuator location. When the pinch and spread planes are aligned, it reduces the Reynolds shear stress.

production. These results need to be validated with future experiments to confirm the numerical findings and interpretations.

SUPPLEMENTARY MATERIAL

The experimental and numerical details and tabulated data are given in the supplementary material.

ACKNOWLEDGMENTS

AUTHOR DECLARATIONS

Conflict of Interest

S.R. has U.S. Patent 10,507,439 issued on December 17, 2019, and U.S. Patent 10,987,640 issued on April 27, 2021.

Ethics Approval

The research meets all ethical guidelines, including adherence to the legal requirements of the study country.

Author Contributions

S.R. conceptualized the research; A.D.G. developed the numerical model and performed simulation; A.D.G. and S.R. analyzed the data and wrote the manuscript.

DATA AVAILABILITY

The data that support the findings of this study are available within the article.

REFERENCES

A. Altıntaş and L. Davidson, "Direct numerical simulation analysis of spanwise oscillating Lorentz force in turbulent channel flow at low Reynolds number," Acta Mech. **228**, 1269–1286 (2017).

P. Andersson, M. Berggren, and D. S. Henningson, "Optimal disturbances and bypass transition in boundary layers," Phys. Fluids **11**, 134–150 (1999).

F. Bassi, A. Crivellini, S. Rebay, and M. Savini, "Discontinuous Galerkin solution of the Reynolds-averaged Navier–Stokes and k–ω turbulence model equations," Comput. Fluids **34**(4), 507–540 (2005).

S. Berlin, A. Lundbladh, and D. Henningson, "Spatial simulations of oblique transition in a boundary layer," Phys. Fluids **6**, 1949–1951 (1994).

A. Bhatia, S. Roy, and R. Gosse, "Effect of dielectric barrier discharge plasma actuators on non-equilibrium hypersonic flows," J. Appl. Phys. **116**, 164904 (2014).

K.-S. Choi, T. Jukes, and R. Whalley, "Turbulent boundary-layer control with plasma actuators," Philos. Trans. R. Soc. London A **369**, 1443–1458 (2011).

A. Das Gupta and S. Roy, "Three-dimensional plasma actuation for faster transition to turbulence," J. Phys. D: Appl. Phys. **50**, 425201 (2017).

Y. Du and G. E. Karniadakis, "Suppressing wall turbulence by means of a transverse traveling wave," Science **288**, 1230–1234 (2000).

R. J. Durscher and S. Roy, "Three dimensional flow measurements induced from serpentine plasma actuators in quiescent air," J. Phys. D: Appl. Phys. **45**, 035202 (2012).

M. E. Goldstein, "Effect of free-stream turbulence on boundary layer transition," Philos. Trans. R. Soc., A **372**, 20130354 (2014).

S. Grundmann and C. Tropea, "Active cancellation of artificially introduced Tollmien–Schlichting waves using plasma actuators," Exp. Fluids **44**, 795–806 (2008).

T. Houba, A. Dasgupta, S. Gopalakrishnan, R. Gosse, and S. Roy, "Supersonic turbulent flow simulation using a scalable parallel modal discontinuous Galerkin numerical method," Sci. Rep. **9**, 14442 (2019).

Kendall, J. M., "Experimental study of disturbances produced in a pre-transitional laminar boundary layer by weak freestream turbulence," in AIAA 18th Fluid Dynamics Plasmadynamics and Lasers Conference, Cincinnati, OH, 1985.

P. S. Klebanoff, "Effect of free-stream turbulence on a laminar boundary layer," Bull. Am. Phys. Soc. **16**, 1323 (1971).

M. Matsubara and P. H. Alfredsson, "Disturbance growth in boundary layers subjected to free-stream turbulence," J. Fluid Mech. **430**, 149–168 (2001).

M. Riherd, S. Roy, and S. Balachandar, "Local stability effects of plasma actuation on a zero pressure gradient boundary layer," Theor. Comput. Fluid Dyn. **28**, 65–87 (2014).

J. R. Roth, D. M. Sherman, and S. P. Wilkinson, "Electrohydrodynamic flow control with a glow discharge surface plasma," AIAA J. **38**, 1166–1172 (2000).

H. Schlichting, Origin of turbulence I, *Boundary-Layer Theory*, 7th ed., (McGraw-Hill, New York, 1979), pp. 454–455.

W. Schoppa and F. Hussain, "Coherent structure generation in near-wall turbulence," J. Fluid Mech. **453**, 57–108 (2002).

K. P. Singh and S. Roy, "Force approximation for a plasma actuator operating in atmospheric air," J. Appl. Phys. **103**, 013305 (2008).

L. Sirovich, "Turbulence and the dynamics of coherent structures. I. Coherent structures," Q. Appl. Math. **45**, 561–571 (1987).

J. J. Wang, K. S. Choi, L. H. Feng, T. N. Jukes, and R. D. Whalley, "Recent developments in DBD plasma flow control," Prog. Aeronaut. Sci. **62**, 52–78 (2013).

A. P. Wheeler, R. D. Sandberg, N. D. Sandham, R. Pichler, V. Michelassi, and G. Laskowski, "Direct numerical simulations of a high-pressure turbine vane," Turbomach. **138**, 071003 (2016).

Wilkinson, S. P., NASA Langley, private communication (2017).

X. Wu, P. Moin, R. J. Adrian, and J. R. Baltzer, "Osborne Reynolds pipe flow: Direct simulation from laminar through gradual transition to fully developed turbulence," Proc. Natl. Acad. Sci. **112**, 7920–7924 (2015).